npj | computational materials

Article

Published in partnership with the Shanghai Institute of Ceramics of the Chinese Academy of Sciences

https://doi.org/10.1038/s41524-026-01961-x

Unraveling the role of Fe and Ni in oxygen evolution reaction on pentlandite using three generations of computational surface models

Maksim Sokolov[1,2,3] & **Kai S. Exner**[1,2,4] ✉

Oxygen evolution reaction (OER)—$2H_2O \rightarrow O_2 + 4H^+ + 4e^-$—remains the primary bottleneck in electrochemical water splitting for green hydrogen production. Pentlandite, a bimetallic chalcogenide mineral, has recently shown promise under alkaline conditions, although the elementary processes at the atomic level remain largely unclear. Using density functional theory calculations, we report three generations of pentlandite surface models with varying complexity to decipher the contributions of Fe and Ni sites to OER activity. The first-generation model is based on the pristine pentlandite surface and purports that no OER catalytic activity is observed. The second-generation model takes surface coverage by adsorbed oxygen or hydroxyl into account and suggests that Fe corresponds to the active site in the OER. In contrast, the third-generation model considers not only the surface coverage but also the surface oxidation of pentlandite by exchanging lattice sulfur atoms with oxygen, as observed experimentally. Only this extension shows that both Fe and Ni sites are active centers for OER and that Fe and Ni exhibit distinct limiting steps depending on applied bias, as determined by a degree of span control analysis. Our results demonstrate that when assessing pentlandite with regard to OER, surface oxidation and coverage effects must be explicitly considered in addition to the mechanistic breadth. The reported modeling approach provides the basis for the rational design of next-generation catalysts by highlighting the importance of considering surface oxidation in the theoretical description of energy conversion processes.

Electrochemical water splitting offers a promising route to green hydrogen production, with the oxygen evolution reaction (OER)—$2H_2O \rightarrow O_2 + 4H^+ + 4e^-$—at the anode representing the main kinetic bottleneck. The sluggish nature of OER arises from its multiple proton-electron transfer steps to form gaseous oxygen under anodic polarization. To address this challenge, there is an urgent need to replace scarce, noble metal-based OER catalysts, such as IrO_2 and RuO_2[1–5], with earth-abundant alternatives that can maintain high activity and long-term stability under harsh alkaline or acidic conditions[6].

Theory has long been viewed as a powerful tool for screening and identifying promising electrocatalyst materials[7]. Early studies by Nørskov, Rossmeisl, and coworkers modeled OER on pristine surface slabs (Fig. 1a, b)—the first-generation model—using a mononuclear description of the elementary reaction steps[8–10]. Over the past two decades, the computational community has moved beyond such simplified models and incorporated other important factors into the identification of promising candidate materials. One of them corresponds to the consideration of surface coverage (Fig. 1c, d), particularly adsorbed oxygen and hydroxyl species, by employing the concept of surface Pourbaix diagrams in second-generation models[11–14]. The inclusion of surface coverage is critical, as it directly influences the energetics of each elementary step and thus the predicted catalytic activity[15–17].

In parallel, the mechanistic understanding has matured beyond a single, mononuclear pathway. Works by Exner and others have shown that bifunctional and Walden-type mechanisms, among others, can compete with or even outperform the traditional mononuclear description when

---

[1]University of Duisburg-Essen, Faculty of Chemistry, Theoretical Catalysis and Electrochemistry, Universitätsstraße 5, Essen, Germany. [2]Cluster of Excellence RESOLV, Bochum, Germany. [3]Institute of Solid State Physics, University of Latvia, Riga, Latvia. [4]Center for Nanointegration (CENIDE) Duisburg-Essen, Duisburg, Germany. ✉e-mail: kai.exner@uni-due.de

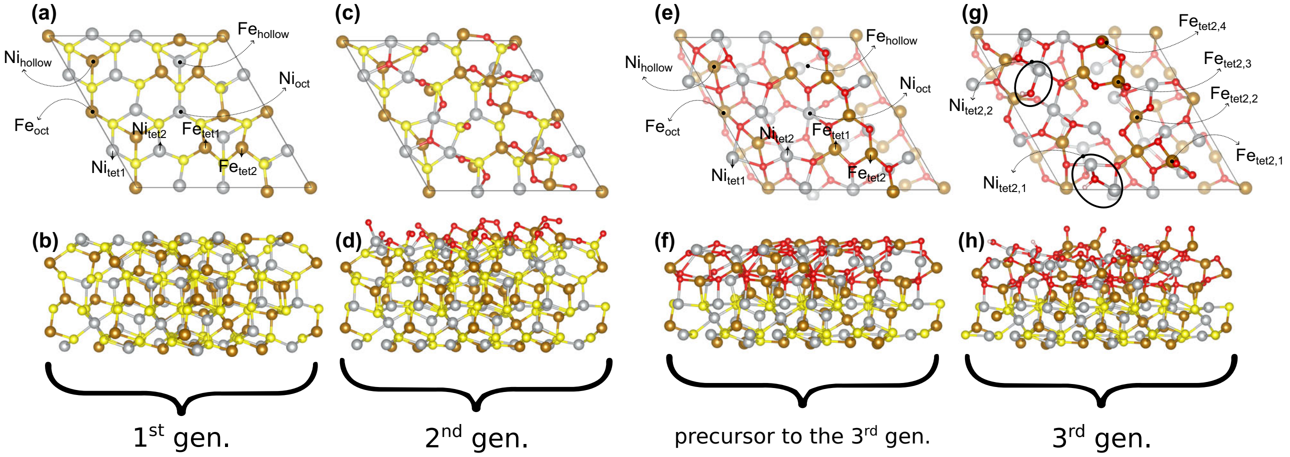

Fig. 1 | Visualization of surface models. The relevant adsorption sites (hollow, oct octahedral, tet tetrahedral) of M = Fe or Ni are marked. **a** Pristine pentlandite, top view of two topmost layers; **b** pristine pentlandite, side view; **c** 20M-O Pourbaix-covered (PC) pentlandite with oxygen adsorbates, top view of the two topmost layers and oxygen coverage; **d** 20M-O Pourbaix-covered (PC) pentlandite, side view; **e** surface-oxidized pentlandite, top view of two topmost layers; **f** surface-oxidized pentlandite, side view; **g** 2M-OH + 6M-O (sub)surface-oxidized Pourbaix-covered (SOPC) pentlandite considering both surface oxidation and surface coverage, top view of two topmost layers and coverage; **h** 2M-OH + 6M-O (sub)surface-oxidized Pourbaix-covered (SOPC) pentlandite, side view.

investigating potential-dependent activity trends[18–23]. Yet, one important aspect remains largely overlooked: surface reconstruction and surface transformations under anodic conditions, including surface oxidation. This is particularly relevant for materials that do not contain oxygen anions in the lattice, such as chalcogenides, phosphides or metallic electrodes. Under anodic polarization, the lattice can transform with the incorporation of oxygen anions, thereby changing the nature and density of the active site and the mechanistic picture.

In the present work, we extend computational models to include surface oxidation under OER conditions using a third-generation model example (Fig. 1e–h) while investigating a single-crystalline pentlandite electrode as a prototypical example. The choice of pentlandite for this study is motivated by experimental works of Apfel and coworkers that demonstrate its high activity and stability for alkaline OER[24,25]. Pentlandite shares similarities with NiFe layered double hydroxides[26] and conductive Ni and Fe-containing hydr(oxy)oxide clusters[27], as in all these materials, the catalytic activity occurs on either Fe or Ni surface sites. Yet pentlandites provide a unique set of challenges in understanding their catalytic properties due to their sulfur content, which leads to a different active phase under reaction conditions compared to Ni and Fe-containing (oxy)hydroxides.

The three different generations of surface models for pentlandite under anodic polarization (cf. Fig. 1) are discussed in the present contribution using methods of electronic structure theory. Notably, only by accounting for surface coverage, surface oxidation, and multiple mechanistic pathways, especially the Walden-type mechanisms that comprise a simultaneous oxygen release and water dissociation step[28], we find that both Fe and Ni tetrahedral sites contribute to the OER activity on the oxidized pentlandite surface. These insights bring theory and experiment to a closer agreement, clarify the electrocatalytic behavior of pentlandites, and also provide general guidelines for the rational design of non-noble metal-based electrocatalysts under anodic polarization.

Results

Three generations of surface structures

To comprehend the elementary steps of the OER on pentlandite (bulk structure unit cell is shown in Fig. S1 in section S1 of the supporting information), we performed density functional theory (DFT) calculations using the computational hydrogen (CHE) framework[8] on three generations of surface models, gradually incorporating an increasing degree of model complexity. Further computational details are provided in the methods section below.

The first-generation model is a pristine pentlandite (111) surface without pre-adsorbed intermediates, shown in Fig. 1a, b. The surface is similar to the model from refs. 16,29, and it is derived from the energetically most favorable metal coordination in the bulk phase (Fig. S1) by additionally taking stoichiometry and slab thickness (>10 Å) requirements into account. The stoichiometry requirement comprises the construction of a surface in such a manner that both surface terminations are similar to avoid an artificial dipole moment, while the stoichiometry in the chemical formula $Fe_{4.5}Ni_{4.5}S_8$ is preserved.

The second-generation surface (Fig. 1c, d) is built upon the first one by considering adsorbate coverage as a result of an applied electrode potential, considering that the OER proceeds for an anodic bias of $U > 1.23$ V vs. RHE (reversible hydrogen electrode)[16]. The inclusion of coverage effects allows an improved description of the electronic structure and chemical environment of the various Ni- and Fe-based active sites on the pentlandite surface. While the surface coverage under anodic potential conditions is commonly attributed to the formation of several M-OH and M-O intermediates (M = Ni or Fe), the exact structure and composition of this coverage are determined by the construction of a surface Pourbaix diagram[12]. We refer to the surface configuration observed at or slightly higher than the equilibrium potential of $U_0^{OER} = 1.23$ V vs. RHE as the Pourbaix coverage (PC). The procedure for determining the PC for pentlandites is an iterative one, as converged structures with lower surface coverage serve as a starting point to determine energetically favorable configurations with higher coverage. This iterative scheme is described in detail in our previous work[16], and the resulting PC for pentlandites refers to a 20M-O surface configuration, where a total of 20 oxygen adsorbates are attached to the different Fe, Ni, and S surface sites of pentlandite's computational cell.

In the present contribution, we introduce a third-generation model that, in addition to surface coverage, takes surface reconstruction of the slab and surface oxidation into account. The starting point of the third-generation surface is the pristine slab, where the top two layers of sulfur (i.e., 50% of all sulfur atoms in the computational cell) are substituted with oxygen (Fig. 1d, e). The corresponding model is called surface-oxidized (SO) pentlandite. There are two main reasons for this model choice: (a) The replacement of sulfur by oxygen in the pentlandite bulk is exergonic, which is further discussed in section S1 of the SI (cf. Table S1). (b) The sulfur-oxygen exchange is corroborated by experimental work of Apfel and coworkers, who indicated that this exchange occurs at sulfur atoms close to the surface[24]: while the upper layers reconstruct, the lower layers are assumed to maintain a conductive pentlanditic core. Hence, we considered both phases

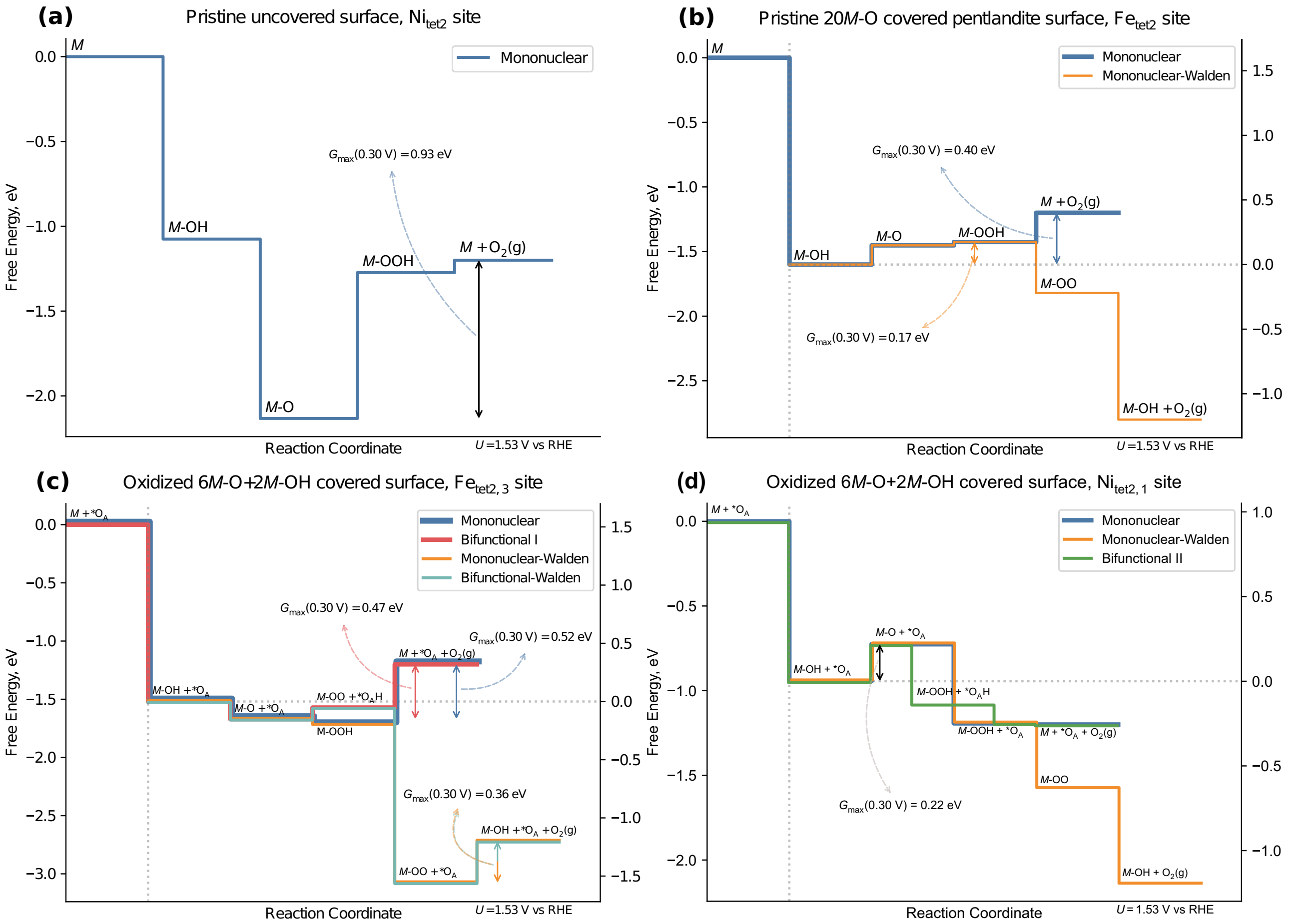

Fig. 2 | Free-energy diagrams (FEDs) for OER on different pentlandite models. Only the most active reaction pathways are shown, where $G_{max}(0.30\ V) < 0.55$ eV is used as a threshold criterion. All FEDs for the various mechanisms are shown in Fig. S3 in section S3 of the SI. **a** Pristine pentlandite surface, first-generation model; **b** Pourbaix-covered (PC) surface, second-generation model; **c** $Fe_{tett2,3}$ site of the (sub)surface-oxidized Pourbaix-covered surface, third-generation model; **d** $Ni_{tett2,1}$ site of the (sub)surface-oxidized Pourbaix-covered surface, third-generation model. In panels (**b**–**d**), the horizontal dotted line refers to the reference for the Walden-type mechanisms and the vertical line to the start of the cycle.

in our slab model (pentlandite at the bottom and oxide on the top), although the oxide phase could potentially be significantly thicker (~100 nm), as reported for mixed metal oxides[30]. Such length scales are beyond the scope of DFT-based methods; therefore, following a common model-system approach in first-principles studies, we employ the half-oxidized slab to capture the essential interplay between the pentlandite core and the oxidized surface.

Since the second layer of sulfur is also relatively exposed and located close to the top of the slab (cf. Fig. 1e, f), we chose two layers instead of one for the substitution of sulfur by oxygen. Subsequently, we apply our recently developed iterative scheme[16] to determine the PC of the SO pentlandite model. The data related to the Pourbaix diagram is condensed in Tables S2 and S3 and Fig. S2 (cf. Section S2 of the SI). We obtain that a 2*M*-OH + 6*M*-O surface configuration—the third-generation model of the (sub)surface-oxidized Pourbaix-covered (SOPC) pentlandite—is energetically favored under OER conditions, as shown in Fig. 1g, h. Please note that the total number of pre-adsorbed intermediates is lower in the third-generation model compared to the second generation. This is mainly due to the fact that the presence of sulfur in the second-generation model provides additional adsorption sites for oxygen intermediates.

The relevance of the SOPC is not limited to the pentlandites discussed in this work, but rather extends to all materials subject to intralayer processes in the electrolyte when bias voltage is applied, such as pure metals (e.g., pure Ir is oxidized to IrO_2 in an electrolyzer) or chalcogenides. The processes involved in the formation of SOPC electrodes include, but are not limited to, surface oxidation, surface reconstruction, and corrosion. A similar model was constructed for the hydrogen evolution reaction on Pd, where H atoms are introduced up to four layers deep into the metallic lattice[31]. Furthermore, surface reconstruction has been shown to play a critical role in OER activity of the Al-doped $La_{0.3}Sr_{0.7}CoO_{3-\delta}$ and $PrBa_{0.5}Sr_{0.5}Co_{2-x}Fe_xO_{5+\delta}$ perovskites[32,33] and in CO electroreduction on Cu (111) in acidic environment[34]. Coincidentally, the inhibiting effect of surface sulfur on oxygen evolution was shown for $Li_{1.2}Ni_{0.6}Mn_{0.2}O_2$ (LNMO), where OER must be suppressed to preserve the material's structural stability[35].

Modeling the catalytic processes on pentlandites

In the next step, we investigate the elementary steps of the OER for the different surface models of Fig. 1. Please note that different tetrahedral and octahedral sites are available on the PC[16] and SOPC pentlandite surfaces. To identify which active sites are relevant for OER, we investigate the stability of a single *M*-OOH intermediate on the pristine or SO surfaces, and only the sites where the *M*-OOH intermediate is stable (Table S2 in section S2 of the SI and ref. 16) are considered for a detailed investigation of the reaction mechanism. The nuance for the PC pentlandite surface is that the precise adsorption location of the reaction intermediates can be better described as an interstitial site between Fe_{tet1} and Fe_{tet2}; nevertheless, we denote it as Fe_{tet2} for the sake of brevity. In addition, the Ni_{tet1} site plays a role in one of the reaction mechanisms. The subtlety for the SOPC surface is that after the derivation of the adsorbate coverage, the symmetry of the sites breaks and the respective four Fe_{tet2} and Ni_{tet2} sites are no longer equivalent. Instead, there are two new $\mathrm{Ni}_{\mathrm{tet2},[1-2]}$ sites and four new $\mathrm{Fe}_{\mathrm{tet2},[1-4]}$ sites (Fig. 1e, g), all of which are considered for a detailed evaluation of the OER mechanism.

Regarding the mechanistic description, we consider the full mechanistic breadth of OER[20] to gain unprecedented insight into the electrocatalytic activity and limiting steps. Besides the conventional mononuclear mechanism[9,10], we account for binuclear[36,37], oxide[23], and bifunctional[21,22,38] descriptions, as well as Walden-type mechanisms[19–21,28,39–41] with concerted desorption-adsorption steps. For this reason, the set of reaction intermediates goes beyond the known OER intermediates M-OH, M-O, and M-OOH by including M-OO and neighboring oxygen sites $^*\mathrm{O}_\mathrm{A}$ near the active center in the analysis. A detailed description of the OER mechanisms and reaction intermediates can be found in the methods section (cf. Equations (2) – (32)).

To analyze the electrocatalytic activity of the different mechanisms for the surface models of Fig. 1, we apply the activity descriptor $G_\mathrm{max}(\eta)$[42,43] based on the energetic span model[44,45], where $\eta = U - U_0^\mathrm{OER}$ refers to the applied overpotential of OER. In the analysis, we choose an applied electrode potential of $U = 1.53$ V vs RHE ($\eta = 0.30$ V), since $\eta = 0.30$ V is related to typical OER overpotentials to achieve a current density on the order of 10 mA/cm^2 [46]. Further details on the derivation of the $G_\mathrm{max}(\eta)$ descriptor can be found in the methods section. Please note that the $G_\mathrm{max}(\eta)$ descriptor is inversely correlated with the electrocatalytic activity, and the heuristic threshold for an active site/mechanism combination is set to $G_\mathrm{max}(0.30\,\mathrm{V}) < 0.55$ eV based on previous work on a similar topic[19]. In Fig. 2, we compile free-energy diagrams (FEDs) for the different models from Fig. 1 by focusing on the most active mechanistic descriptions using $G_\mathrm{max}(0.30\,\mathrm{V}) < 0.55$ eV, although the pristine pentlandite surface corresponding to the first-generation model does not show sufficient OER activity (Fig. 2a). Details for all investigated mechanisms and FED plots for other pathways and surface sites are provided in Tables S4 and S5 and Fig. S3 of the SI, respectively (cf. section S3).

While for the pristine pentlandite surface only the mononuclear mechanism was investigated (Fig. 2a)[16], it was concluded that the first-generation model is overall inactive for OER due to the unreasonably high $G_\mathrm{max}(0.30\,\mathrm{V})$ value, which contradicts the experimental data[24,25]. If we distinguish between Fe and Ni as active sites for the pristine pentlandite surface, we conclude that the $\mathrm{Ni}_\mathrm{tet2}$ site is the most active with $G_\mathrm{max}(0.30\,\mathrm{V}) = 0.93$eV.

The situation drastically changes once we take the PC in the second-generation model into account[16], as depicted in Fig. 2b. In this case, while the $\mathrm{Ni}_\mathrm{tet2}$ remains relatively inactive for OER ($G_\mathrm{max}(0.30\,\mathrm{V}) = 0.64$ eV), the $\mathrm{Fe}_\mathrm{tet2}$ site demonstrates remarkable activity with $G_\mathrm{max}(0.30\,\mathrm{V}) = 0.40$ eV and 0.17eV for the mononuclear and mononuclear-Walden mechanisms, respectively (for more details, see Table S4 in section S3 of the SI). Note that the mononuclear-Walden mechanism has the potential to be more active than its traditional counterpart only in case the elementary step of M-OOH $\rightarrow M + \mathrm{O}_2$ (g) is present in the rate-determining span (i.e., the largest span in the FED or, equivalently, the span that defines the $G_\mathrm{max}(\eta)$ descriptor) of the mononuclear mechanism. This condition is met on the $\mathrm{Fe}_\mathrm{tet2}$ of the PC surface, and due to the exergonic nature of the transition M-OOH $\rightarrow M$-OO $+ \mathrm{H}^+ + \mathrm{e}^-$ on this site, the mononuclear mechanism is outperformed by its Walden counterpart. As is evident from the $G_\mathrm{max}(0.30\,\mathrm{V})$ values from Tables S4 and S5, and FEDs from Fig. S3 in section S3 of the SI, the other mechanisms are proven to have only a limited impact on the OER activity.

The discussion of the reaction mechanism and electrocatalytic activity is even more nuanced and complex on the third-generation SOPC surface. Instead of one distinguished active site on the surface as in previous cases, now there are two sites of two different metal species, indexed as $\mathrm{Fe}_{\mathrm{tet2},3}$ (Fig. 2c) and $\mathrm{Ni}_{\mathrm{tet2},1}$ (Fig. 2d), competing with each other under anodic polarization. This represents a significant change in the OER description over pentlandites compared to the first- and second-generation models. Another shift is observed by comparing the rate-determining spans between panels b, c of Fig. 2: it changes from M-OH $\rightarrow M + \mathrm{O}_2$ (g) and M-OH $\rightarrow M$-OOH to M-O $\rightarrow M + \mathrm{O}_2$ (g) and M-OO $\rightarrow M$-OH $+ \mathrm{O}_2$ (g) for the mononuclear and mononuclear-Walden mechanisms, respectively. Furthermore, the mechanistic variety becomes more diverse, with mononuclear, bifunctional I and Walden-type mechanisms being active on the $\mathrm{Fe}_{\mathrm{tet2},3}$ site, whereas mononuclear, mononuclear-Walden, and bifunctional II mechanisms are prevalent on the $\mathrm{Ni}_{\mathrm{tet2},1}$ site. Finally, for the SOPC, $\mathrm{Ni}_{\mathrm{tet2},1}$ was found to have a higher activity ($G_\mathrm{max}(0.30\,\mathrm{V}) = 0.22$ eV for all three active mechanisms) than the $\mathrm{Fe}_{\mathrm{tet2},3}$ (lowest $G_\mathrm{max}(0.30\mathrm{V}) = 0.36$ eV) site, albeit both values are slightly higher than for the mononuclear-Walden mechanism on the PC surface. Although the activity described by $G_\mathrm{max}(0.30\,\mathrm{V})$ remains similar between the PC and SOPC surfaces, the activity of the latter might be higher due to the higher density of active sites, as both Fe and Ni species contribute to the formation of gaseous oxygen.

Active sites of pentlandites under anodic polarization

In Fig. 3, we provide an evolution of the OER description and active sites on pentlandites as we move across three generations of surface models. It clearly demonstrates the need to consider both the adsorbate coverage and surface oxidation, as the conclusions for pristine, PC, and SOPC surfaces shift from "no activity" to "Fe species is active" to "Ni and Fe are active sites", respectively. While both the PC and SOPC models align with the experimental data regarding a qualitative assessment of OER activity, the SOPC further improves the description, which we relate to the experimentally observed change in OER activity with different Ni:Fe stoichiometry: with increasing Ni content, OER activity increases[24]. Thus, the simplest explanation for that would be that Ni must contribute to the activity and provide active surface sites, and only the SOPC model confirms this finding. Note that this does not mean that Fe is inactive; rather, both species contribute to activity.

Regarding the mechanistic description, we find that Walden-type mechanisms consistently improve OER activity or stay on par with their non-Walden counterparts. A similar observation was made previously for electrochemically formed single-atom centers of *MX*enes[19] and for $\mathrm{Co}_3\mathrm{O}_4$[20]: there, the Walden-type mechanisms showed higher activity or remained at the same level, even if the condition that the elementary step M-OOH $\rightarrow M + \mathrm{O}_2$ (g) is part of the rate-determining span was not fulfilled.

Mechanistic pathway and elementary step contributions to the overall current density

To further comprehend the mechanistic details of the OER on the SOPC surface, we apply the concept of degree of span control (DSC), as recently introduced by ref. 20. While the discussion of the electrocatalytic activity in computational studies is often based on the identification of a single elementary reaction step using the notion of the potential-determining step[47], several reaction mechanisms and elementary steps can contribute to the reaction rate to varying degrees depending on the applied overpotential. The DSC analysis takes this fact into account by means of a potential-dependent sensitivity analysis reminiscent of Campbell's degree of span control[48,49], although the DSC concept does not require the calculation of transition states and remains on the level of thermodynamic considerations. Further details on the DSC concept are provided in the methods section.

The DSC concept is exerted on the two active sites of the SOPC surface. For $\mathrm{Fe}_{\mathrm{tet2},3}$, bifunctional I, bifunctional-Walden, and mononuclear-Walden mechanisms are shown to be active (Fig. 4a), which is consistent with the previously defined activity threshold of $G_\mathrm{max}(0.30\mathrm{V}) < 0.55$ eV (except for the mononuclear mechanism, which does not appear in the plots due to the exponential nature of DSC and its slightly higher G_max). For the active mechanisms, two different free-energy spans are limiting the OER activity, namely M-OO $\rightarrow M$-OH $+ \mathrm{O}_2$(g) and M-OO $\rightarrow M + \mathrm{O}_2$(g) for Walden-type and bifunctional mechanisms, respectively (Fig. 4b). Please note that the partial contributions to the DSC_m (m = mechanism) and DSC_j (j = span) descriptions flatten and become horizontal once all three mechanisms are controlled by a single electron transfer step; this is observed at about $U \approx 1.62$ V vs RHE. While the Walden step M-OO $\rightarrow M$-OH $+ \mathrm{O}_2$(g) mainly limits the electrocatalytic activity of the $\mathrm{Fe}_{\mathrm{tet2},3}$ site, it becomes evident that the notion of a single limiting reaction step is not fulfilled at high overpotentials (Fig. 4b).

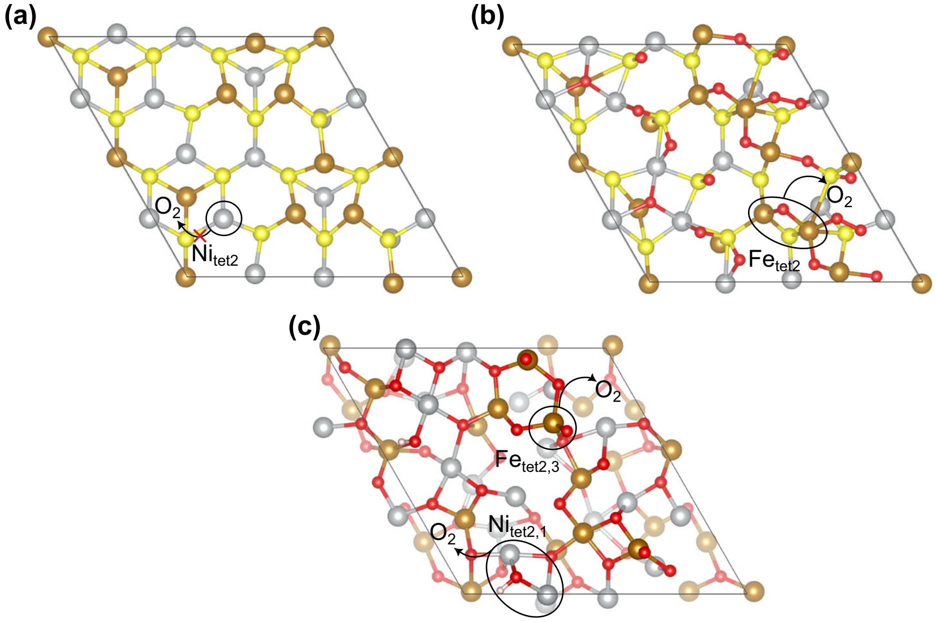

Fig. 3 | Visualization of the OER on the three generations of surface models. Brown spheres—Fe atoms, gray spheres—Ni atoms, yellow spheres—S atoms, red spheres—O atoms, white spheres—H atoms. **a** The pristine pentlandite surface, first generation. **b** Pourbaix-covered surface, second generation. **c** (Sub)surface-oxidized Pourbaix-covered surface, third generation.

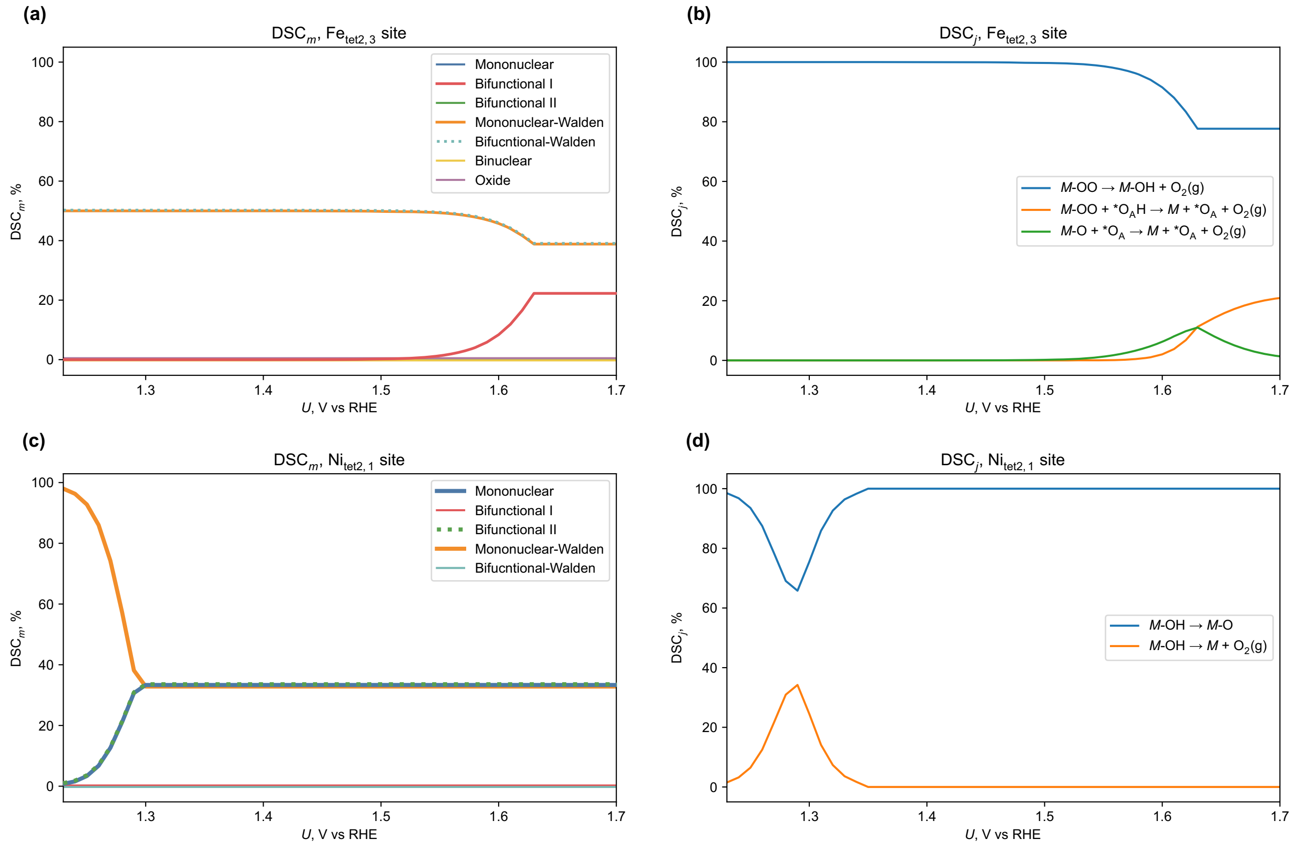

Fig. 4 | Visualization of the degree of span control (DSC) on the (sub)surface-oxidized Pourbaix-covered pentlandite surface, third-generation model. DSC_m indicates the contribution of different reaction mechanisms for a particular active site to the current density, DSC_j indicates the contribution of different spans based on the preferred reaction mechanisms to the current density. **a** DSC_m on the $Fe_{tet2,3}$ site; **b** DSC_j on the $Fe_{tet2,3}$ site; **c** DSC_m on the $Ni_{tet2,1}$ site; **d** DSC_j on the $Ni_{tet2,1}$ site.

A similar correlation between the FEDs and DSC plots is observed for the active $Ni_{tet2,1}$ site, where the DSC_m plot is governed by mononuclear, mononuclear-Walden, and bifunctional II mechanisms, all of which have equal contributions to the reaction rate for $U > 1.30$ V vs RHE (Fig. 4c). For all three mechanisms, the formation of surface oxygen—$M\text{-}OH \rightarrow M\text{-}O$—is identified as the limiting one for $U > 1.30$ V vs RHE (Fig. 4d), indicating that the picture of a single limiting step is fulfilled for the active $Ni_{tet2,1}$ site.

Discussion

In the present work, we highlight the importance of surface oxidation for the modeling of electrodes relevant for proton-coupled electron transfer steps, using a pentlandite model in the oxygen evolution reaction as a prototypical example. To reach this stage, we compare the results of three generations of computational surface models and compare them to the available experimental data. While the first-generation model is based on a pristine pentlandite slab, the second- and third-generation models consider the adsorbate coverage as well as the surface oxidation and adsorbate coverage, respectively.

While the results of the pristine surface model indicate that pentlandites are inactive for OER, both second- and third-generation models confirm that pentlandite is an active electrocatalyst, which is consistent with experiments. The main difference between the second- and third-generation models concerns the identification of active sites under anodic polarization. While the second-generation model shows that tetrahedral Fe appears to be the unique active site, only by considering surface oxidation can we show that both tetrahedral Fe and Ni sites contribute to OER activity. The identification of both surface Fe and Ni as active centers for OER agrees with experimental data when considering activity trends with different Ni:Fe stoichiometry: higher Ni content leads to higher activity. Therefore, the second-generation model, which omits surface oxidation, underestimates the density of active surface sites and identifies a different reaction mechanism than the third-generation model.

The proposed methodology of incorporating surface coverage, surface oxidation, and multiple reaction mechanisms into the analysis of proton-coupled electron transfer steps is key to bringing theoretical models closer to experimental investigations, although the exact surface structure in operando remains unresolved. Surface oxidation —and other effects such as corrosion and surface reconstruction—has so far received little attention in computational works on electrocatalysis. We believe that the present work can stimulate the application of improved computational surface models to unambiguously identify active sites, reaction mechanisms, and limiting reaction steps under applied bias voltage.

Methods

Computational details

We performed electronic structure theory calculations in the density functional theory (DFT) framework as implemented in VASP[50]. Table S6 in section S4 of the SI summarizes the computational details to obtain the presented results. For the complete setup, we refer to the data repository, which contains all the necessary information to fully reproduce our calculations[51].

Potential-dependent Gibbs free energies for surface configurations are calculated using the computational hydrogen electrode (CHE) method[8]:

$$G = E_{\mathrm{DFT}} + E_{\mathrm{ZPE}} - TS - n_e eU \tag{1}$$

Here, n_e denotes the number of electron transfers in the reaction mechanism preceding the reaction intermediate, e is the elementary charge, and U is the applied electrode potential on the RHE scale (reversible hydrogen electrode). All surface calculations of E_{DFT} were performed using the RPBE functional[52,53] with the D3 correction to account for van der Waals forces[54,55], and only the positions of the bottom slab layer were fixed and not allowed to relax. The E_{ZPE} and TS are only considered for the gas-phase molecules H_2O and H_2, E_{ZPE} is calculated via the finite-difference method in VASP at $E_{\mathrm{ZPE}}(H_2O) = 0.55\,\mathrm{eV}$ and $E_{\mathrm{ZPE}}(H_2) = 0.19\,\mathrm{eV}$, and the TS term is sourced from standard thermodynamic tables at $TS(H_2O) = 0.67\,\mathrm{eV}$ and $TS(H_2) = 0.40\,\mathrm{eV}$[56]. In order to maintain computational resources, we assume that the E_{ZPE} and TS terms approximately cancel out between reaction steps and do not impact the qualitative picture. This assumption is justified based on the data shown for the PC surface in Table S5 (cf. section S4 of the SI).

Spin polarization effects were neglected, as pentlandite is not known to exhibit magnetic behavior[57]. The Hubbard U correction, which is often applied to mitigate the self-interaction error present in GGA-type functionals such as RPBE and to improve d-electron localization, was also omitted. This choice aligns with previously benchmarked adsorption energy results that did not employ a Hubbard U correction[58,59]. Although the importance of the Hubbard U correction was demonstrated for constructing precise Pourbaix diagrams[60], its general applicability is still debated[61] and is hard to validate for pentlandites, which are metallic[24]. Moreover, our test calculations indicated that including spin polarization or the Hubbard U correction substantially slows down geometry relaxations[51].

In addition, solvent effects were not explicitly or implicitly modeled. This decision was based on prior benchmarks[16], which showed that simple solvation models—either implicit representations or those including one to two explicit water molecules—have only minor effects on the adsorption free energies relevant for catalytic activity. To truly capture the solvation effects, the structure of the first solvation shell and an appropriate number of explicit water molecules are required, which is beyond the scope of the present work.

In order to qualitatively support the 3rd generation model, we performed the Bader charge analysis[62] (section S5 of the SI), which shows a higher charge on active species of the 3rd generation model compared to the second. This increase in charge clearly indicates a generally higher surface charge in the third-generation system, qualitatively aligning it more closely with the experimentally observed +III or even +IV oxidation states of Fe and Ni under OER conditions in non-pentlandite materials[63].

OER mechanisms

In Eqs. (2)–(32), we provide the mechanistic descriptions for the mononuclear[9,10], bifunctional I[22], bifunctional II[21,22,38], binuclear[36,37], oxide[23], mononuclear-Walden[19,20,28,39–41], and bifunctional-Walden[19,20] mechanisms. Walden-type mechanisms have been gaining importance recently, as they were demonstrated to be relevant for IrO_2[41]. In the following equations, M denotes an active surface site, i.e., Fe or Ni, and $\Delta G_{m,i}$ denotes the corresponding free-energy change of mechanism m (abbreviated) at index i.

a) Mononuclear mechanism[9,10]

$$M + H_2O \rightarrow M\text{-OH} + H^+ + e^- \;\; \Delta G_{\mathrm{mn},1} \tag{2}$$

$$M\text{-OH} \rightarrow M\text{-O} + H^+ + e^- \;\; \Delta G_{\mathrm{mn},2} \tag{3}$$

$$M\text{-O} + H_2O \rightarrow M\text{-OOH} + H^+ + e^- \;\; \Delta G_{\mathrm{mn},3} \tag{4}$$

$$M\text{-OOH} \rightarrow M + O_2(g) + H^+ + e^- \;\; \Delta G_{\mathrm{mn},4} \tag{5}$$

b) Bifunctional mechanism I[22]

$$M + {}^*O_A + H_2O \rightarrow M\text{-OH} + {}^*O_A + H^+ + e^- \;\; \Delta \mathrm{G}_{\mathrm{bfI},1} \tag{6}$$

$$M\text{-OH} + {}^*O_A \rightarrow \mathrm{M}\text{-O} + {}^*O_A + H^+ + e^- \;\; \Delta \mathrm{G}_{\mathrm{bfI},2} \tag{7}$$

$$M\text{-O} + {}^*O_A + H_2O \rightarrow M\text{-OO} + {}^*O_AH + H^+ + e^- \;\; \Delta \mathrm{G}_{\mathrm{bfI},3} \tag{8}$$

$$M\text{-OO} + {}^*O_AH \rightarrow \mathrm{M} + {}^*O_A + O_2(g) + H^+ + e^- \;\; \Delta \mathrm{G}_{\mathrm{bfI},4} \tag{9}$$

c) Bifunctional mechanism II[21,22,38]

$$M + {}^*O_A + H_2O \rightarrow M\text{-OH} + {}^*O_A + H^+ + e^- \;\; \Delta \mathrm{G}_{\mathrm{bfII},1} \tag{10}$$

$$M\text{-OH} + {}^*O_A \rightarrow \mathrm{M}\text{-O} + {}^*O_A + H^+ + e^- \;\; \Delta \mathrm{G}_{\mathrm{bfII},2} \tag{11}$$

$$M\text{-O} + {}^*O_A + H_2O \rightarrow M\text{-OOH} + {}^*O_AH \;\; \Delta \mathrm{G}_{\mathrm{bfII},3} \tag{12}$$

$$M\text{-OOH} + {}^*O_AH \rightarrow \mathrm{M}\text{-OOH} + {}^*O_A + H^+ + e^- \;\; \Delta \mathrm{G}_{\mathrm{bfII},4} \tag{13}$$

$$M\text{-OOH} + {}^*O_A \rightarrow \mathrm{M} + {}^*O_A + O_2(g) + H^+ + e^- \;\; \Delta \mathrm{G}_{\mathrm{bfII},5} \tag{14}$$

d) Binuclear mechanism[36,37]

$$M + M + \mathrm{H_2O} \rightarrow M\text{-OH} + M + \mathrm{H^+} + \mathrm{e^-}\ \Delta G_{\mathrm{bn},1} \tag{15}$$

$$M\text{-OH} + M + \mathrm{H_2O} \rightarrow M\text{-OH} + M\text{-OH} + \mathrm{H^+} + \mathrm{e^-}\ \Delta G_{\mathrm{bn},2} \tag{16}$$

$$M\text{-OH} + M - \mathrm{OH} \rightarrow M\text{-O} + M\text{-OH} + \mathrm{H^+} + \mathrm{e^-}\ \Delta G_{\mathrm{bn},3} \tag{17}$$

$$M\text{-O} + M\text{-OH} \rightarrow M\text{-O} + M\text{-O} + \mathrm{H^+} + \mathrm{e^-}\ \Delta G_{\mathrm{bn},4} \tag{18}$$

$$M\text{-O} + M\text{-O} \rightarrow M + M + \mathrm{O_2(g)}\ \Delta G_{\mathrm{bn},5} \tag{19}$$

e) Oxide mechanism[23]

$$M\text{-O} + M\text{-O} + \mathrm{H_2O} \rightarrow M\text{-OOH} + M\text{-O} + \mathrm{H^+} + \mathrm{e^-}\ \Delta G_{\mathrm{ox},1} \tag{20}$$

$$M\text{-OOH} + M\text{-O} + \mathrm{H_2O} \rightarrow M\text{-OOH} + M\text{-OOH} + \mathrm{H^+} + \mathrm{e^-}\ \Delta G_{\mathrm{ox},2} \tag{21}$$

$$M\text{-OOH} + M\text{-OOH} \rightarrow M\text{-OOH} + M\text{-OO} + \mathrm{H^+} + \mathrm{e^-}\ \Delta G_{\mathrm{ox},3} \tag{22}$$

$$M\text{-OOH} + M\text{-OO} \rightarrow M\text{-OO} + M\text{-OO} + \mathrm{H^+} + \mathrm{e^-}\ \Delta G_{\mathrm{ox},4} \tag{23}$$

$$M\text{-OO} + M\text{-OO} \rightarrow M\text{-O} + M\text{-O} + \mathrm{O_2(g)}\ \Delta G_{\mathrm{ox},5} \tag{24}$$

f) Mononuclear-Walden mechanism[19,20,28,39–41]

$$M\text{-OH} \rightarrow M\text{-O} + \mathrm{H^+} + \mathrm{e^-}\ \Delta G_{\mathrm{mw},1} \tag{25}$$

$$M\text{-O} + \mathrm{H_2O} \rightarrow M\text{-OOH} + \mathrm{H^+} + \mathrm{e^-}\ \Delta G_{\mathrm{mw},2} \tag{26}$$

$$M\text{-OOH} \rightarrow M\text{-OO} + \mathrm{H^+} + \mathrm{e^-}\ \Delta G_{\mathrm{mw},3} \tag{27}$$

$$M\text{-OO} + \mathrm{H_2O} \rightarrow M\text{-OH} + \mathrm{H^+} + \mathrm{e^-} + \mathrm{O_2(g)}\ \Delta G_{\mathrm{mw},4} \tag{28}$$

g) Bifunctional-Walden mechanism[19,20]

$$M\text{-OH} + {}^*\mathrm{O_A} \rightarrow \mathrm{M\text{-}O} + {}^*\mathrm{O_A} + \mathrm{H^+} + \mathrm{e^-}\ \Delta \mathrm{G}_{\mathrm{bw},1} \tag{29}$$

$$M\text{-O} + {}^*\mathrm{O_A} + \mathrm{H_2O} \rightarrow M\text{-OO} + {}^*\mathrm{O_AH} + \mathrm{H^+} + \mathrm{e^-}\ \Delta G_{\mathrm{bw},2} \tag{30}$$

$$M\text{-OO} + {}^*\mathrm{O_AH} \rightarrow \mathrm{M\text{-}OO} + {}^*\mathrm{O_A} + \mathrm{H^+} + \mathrm{e^-}\ \Delta G_{\mathrm{bw},3} \tag{31}$$

$$M\text{-OO} + {}^*\mathrm{O_A} + \mathrm{H_2O} \rightarrow \mathrm{M\text{-}OH} + {}^*\mathrm{O_A} + \mathrm{H^+} + \mathrm{e^-} + \mathrm{O_2(g)}\ \Delta \mathrm{G}_{\mathrm{bw},4} \tag{32}$$

The free energy change for the elementary step can be expressed by the free energy of the reaction intermediates—$G_{m,i}$—involved. Note that m refers to a specific mechanism (see Eqs. (2) – (32)), and i denotes the index of the respective elementary step in this mechanism. As evident from the above, $1 \le i \le 4$ for the mononuclear and bifunctional I mechanisms, including their Walden descriptions, while $1 \le i \le 5$ holds for the bifunctional II, binuclear, and oxide pathways due to a chemical step in the catalytic cycle.

$$\Delta G_{m,i} = G_{m,i} - G_{m,(i-1)} \tag{33}$$

Please note that the last free energy change of each mechanism corresponds to the formation and release of gaseous oxygen. This step is not calculated with DFT, but rather we apply the concept of gas-phase error corrections[64,65] to meet the experimental equilibrium potential of OER:

$$\Delta G_{m,i_{\max}} = 4.92 - \sum_{i=1}^{i_{\max}-1} \Delta G_{m,i} \tag{34}$$

Finally, we note that the reaction mechanisms above represent an acidic environment rather than an alkaline one. In the framework of a descriptor-based analysis using the CHE approach, the free-energy changes do not depend on pH[66], as this would require a grand canonical formalism, which is beyond the scope of this work.

Activity descriptor $G_{\max}(\eta)$

The activity descriptor $G_{\max}(\eta)$ [42,43] based on the energetic span model for a given mechanism is defined in its compact form as follows[67]:

$$G_{\max,m}(\eta) = \max\{S_{m,j}\} = \max\left\{\sum_{i=k}^{i=l} \Delta G_{m,i}\right\} \tag{35}$$

It is selected as a more precise alternative to the conventional thermodynamic overpotential, η_{TD}[8]. While the latter is defined as the largest step in the free-energy diagram at the equilibrium potential, the former is a potential-dependent proxy of the electrocatalytic activity based on the energetic span model, and thus is more suitable for the description of non-equilibrium electrochemical processes such as OER. Here, $S_{m,j}$ denote all possible free energy spans of that mechanism, which are calculated based on all possible combinations of the free energy changes of the elementary steps. In case of $1 \le i \le 4$ (mononuclear, bifunctional I, mononuclear-Walden, and bifunctional-Walden mechanisms), the number of total spans ($j_{\max}$) amounts to 10, whereas for $1 \le i \le 5$ (bifunctional II, binuclear and oxide mechanisms), we observe $j = 15$. The largest free energy span at a given overpotential η is reconciled with the $G_{\max,m}(\eta)$ descriptor of mechanism m. Note that the applied OER overpotential is defined as $\eta = U - U_0^{\mathrm{OER}}$ with $U_0^{\mathrm{OER}} = 1.23$ V vs RHE (reversible hydrogen electrode).

Degree of span control (DSC)

In the Tafel regime, the partial current density j_m of each reaction mechanism m based on the $G_{\max,m}(\eta)$ descriptor for that mechanism can be expressed as follows[17]:

$$j_m(\eta) \sim \exp\left[\frac{-G_{\max,m}(\eta)}{k_B T}\right] \tag{36}$$

The total current density j corresponds to the sum of all partial current densities for all mechanisms m:

$$j(\eta) = \sum_m j_m(\eta) \tag{37}$$

The degree of span control for a particular mechanism m, denoted DSC_m, is defined as its relative contribution to the overall current density:

$$\mathrm{DSC}_m(\eta) = \frac{j_m(\eta)}{j(\eta)} \tag{38}$$

To determine the contribution of individual spans $S_{m,j}$ for a given mechanism m, we introduce the term $\mathrm{DSC}_{m,j}$:

$$\mathrm{DSC}_{m,j}(\eta) = \frac{\exp\left(\frac{+S_{m,j}(\eta)}{k_B T}\right)}{\sum_j \exp\left(\frac{+S_{m,j}(\eta)}{k_B T}\right)} \mathrm{DSC}_m(\eta) \tag{39}$$

Based on Eq. (39), we can determine the impact of each span j among all mechanisms m to the current density by using the relation in Eq. (40):

$$\mathrm{DSC}_j = \sum\nolimits_m \mathrm{DSC}_{m,j}(\eta) \tag{40}$$

DSC_m and DSC_j are used to investigate the contribution of the different mechanisms and spans for the active Fe and Ni sites of the third-generation pentlandite model in Fig. 4.

Data availability

All data supporting the findings of this study are available at the following URL: M. Sokolov, Kai S. Exner, Data repository and scripts for the OER on pentlandite DFT calculations. https://doi.org/10.5281/zenodo.17554150. Deposited 7 November 2025.

Received: 10 July 2025; Accepted: 7 January 2026;
Published online: 22 January 2026

References

1. Over, H. Fundamental studies of planar single-crystalline oxide model electrodes (RuO_2, IrO_2) for acidic water splitting. *ACS Catal.* **11**, 8848–8871 (2021).
2. Stoerzinger, K. A., Qiao, L., Biegalski, M. D. & Shao-Horn, Y. Orientation-dependent oxygen evolution activities of rutile IrO_2 and RuO_2. *J. Phys. Chem. Lett.* **5**, 1636–1641 (2014).
3. Lim, H. Y., Park, S. O., Kim, S. H., Jung, G. Y. & Kwak, S. K. First-principles design of rutile oxide heterostructures for oxygen evolution reactions. *Front. Energy Res.* **9**, 606313 (2021).
4. Kuo, D.-Y. et al. Influence of surface adsorption on the oxygen evolution reaction on IrO_2 (110). *J. Am. Chem. Soc.* **139**, 3473–3479 (2017).
5. Kuo, D.-Y. et al. Measurements of oxygen electroadsorption energies and oxygen evolution reaction on RuO_2 (110): a discussion of the Sabatier principle and its role in electrocatalysis. *J. Am. Chem. Soc.* **140**, 17597–17605 (2018).
6. Xu, S. et al. Developing new electrocatalysts for oxygen evolution reaction via high throughput experiments and artificial intelligence. npj Comput. *npj Comput. Mater.* **10**, 194 (2024).
7. Li, Z. et al. Interpreting chemisorption strength with AutoML-based feature deletion experiments. *Proc. Natl. Acad. Sci. USA* **121**, e2320232121 (2024).
8. Nørskov, J. K. et al. Origin of the overpotential for oxygen reduction at a fuel-cell cathode. *J. Phys. Chem. B* **108**, 17886–17892 (2004).
9. Rossmeisl, J., Logadottir, A. & Nørskov, J. K. Electrolysis of water on (oxidized) metal surfaces. *Chem. Phys.* **319**, 178–184 (2005).
10. Rossmeisl, J., Qu, Z.-W., Zhu, H., Kroes, G.-J. & Nørskov, J. K. Electrolysis of water on oxide surfaces. *J. Electroanal. Chem.* **607**, 83–89 (2007).
11. Pourbaix, M. Some applications of electrochemical thermodynamics. *Corrosion* **6**, 395–404 (1950).
12. Hansen, H. A., Rossmeisl, J. & Nørskov, J. K. Surface Pourbaix diagrams and oxygen reduction activity of Pt, Ag and Ni(111) surfaces studied by DFT. *Phys. Chem. Chem. Phys.* **10**, 3722 (2008).
13. Exner, K. S. Constrained ab initio thermodynamics: transferring the concept of surface Pourbaix diagrams in electrocatalysis to electrode materials in lithium-ion batteries. *ChemElectroChem* **4**, 3231–3237 (2017).
14. Wang, Z., Guo, X., Montoya, J. & Norskov, J. K. Predicting aqueous stability of solid with computed Pourbaix diagram using SCAN functional. npj Comput. *npj Comput. Mater.* **6**, 160 (2020).
15. Ciotti, A. & García-Melchor, M. The importance of surface coverages in the rational design of electrocatalysts. *Curr. Opin. Electrochem.* **42**, 101402 (2023).
16. Sokolov, M., Doblhoff-Dier, K. & Exner, K. S. Best practices of modeling complex materials in electrocatalysis, exemplified by oxygen evolution reaction on pentlandites. *Phys. Chem. Chem. Phys.* **26**, 22359–22370 (2024).
17. Morankar, A., Deshpande, S., Zeng, Z., Atanassov, P. & Greeley, J. A first principles analysis of potential-dependent structural evolution of active sites in Fe-N-C catalysts. *Proc. Natl. Acad. Sci. USA* **120**, e2308458120 (2023).
18. Exner, K. S. On the mechanistic complexity of oxygen evolution: potential-dependent switching of the mechanism at the volcano apex. *Mater. Horiz.* **10**, 2086–2095 (2023).
19. Razzaq, S. et al. MXenes spontaneously form active and selective single-atom centers under anodic polarization conditions. *J. Am. Chem. Soc.* **147**, 161–168 (2025).
20. Dhaka, K. & Exner, K. S. Degree of span control to determine the impact of different mechanisms and limiting steps: oxygen evolution reaction over Co3O4(001) as a case study. *J. Catal.* **443**, 115970 (2025).
21. Fang, Y.-H. & Liu, Z.-P. Mechanism and Tafel lines of electro-oxidation of water to oxygen on RuO_2 (110). *J. Am. Chem. Soc.* **132**, 18214–18222 (2010).
22. Halck, N. B., Petrykin, V., Krtil, P. & Rossmeisl, J. Beyond the volcano limitations in electrocatalysis – oxygen evolution reaction. *Phys. Chem. Chem. Phys.* **16**, 13682–13688 (2014).
23. Binninger, T. & Doublet, M.-L. The Ir–OOOO–Ir transition state and the mechanism of the oxygen evolution reaction on IrO_2 (110). *Energy Environ. Sci.* **15**, 2519–2528 (2022).
24. Amin, H. M. A., Attia, M., Tetzlaff, D. & Apfel, U. Tailoring the electrocatalytic activity of pentlandite $Fe_xNi_{9-X}S_8$ nanoparticles via variation of the Fe:Ni ratio for enhanced water oxidation. *ChemElectroChem* **8**, 3863–3874 (2021).
25. Hegazy, M. B. Z. et al. Boosting the overall electrochemical water splitting performance of pentlandites through non-metallic heteroatom incorporation. *iScience* **25**, 105148 (2022).
26. Dionigi, F. et al. In-situ structure and catalytic mechanism of NiFe and CoFe layered double hydroxides during oxygen evolution. *Nat. Commun.* **11**, 2522 (2020).
27. Chung, D. Y. et al. Dynamic stability of active sites in hydr(oxy)oxides for the oxygen evolution reaction. *Nat. Energy* **5**, 222–230 (2020).
28. Exner, K. S. Importance of the Walden inversion for the activity volcano plot of oxygen evolution. *Adv. Sci.* **10**, 2305505 (2023).
29. Waterson, C. N., Sindt, J. O., Cheng, J., Tasker, P. & Morrison, C. First-principles study on ligand binding and positional disorder in pentlandite. *J. Phys. Chem. C* **119**, 25457–25468 (2015).
30. Samira, S. et al. Dynamic surface reconstruction unifies the electrocatalytic oxygen evolution performance of nonstoichiometric mixed metal oxides. *JACS Au* **1**, 2224–2241 (2021).
31. Schmidt, T. O. et al. Elucidation of structure–activity relations in proton electroreduction at Pd surfaces: theoretical and experimental study. *Small* **18**, 2202410 (2022).
32. Wei, Y. et al. Triggered lattice-oxygen oxidation with active-site generation and self-termination of surface reconstruction during water oxidation. *Proc. Natl. Acad. Sci. USA* **120**, e2312224120 (2023).
33. Jo, H. et al. Promotion of the oxygen evolution reaction via the reconstructed active phase of perovskite oxide. *J. Mater. Chem. A* **10**, 2271–2279 (2022).
34. Cheng, D., Alexandrova, A. N. & Sautet, P. H-induced restructuring on Cu(111) triggers CO electroreduction in an acidic electrolyte. *J. Phys. Chem. Lett.* **15**, 1056–1061 (2024).

35. Lin, K. -Y., Nachimuthu, S., Huang, H. -W. & Jiang, J. -C. Theoretical insights on alleviating lattice-oxygen evolution by sulfur substitution in Li1.2Ni0.6Mn0.2O2 cathode material. npj Comput. *npj Comput. Mater.* **8**, 210 (2022).
36. Busch, M., Ahlberg, E. & Panas, I. Electrocatalytic oxygen evolution from water on a Mn(iii–v) dimer model catalyst—a DFT perspective. *Phys. Chem. Chem. Phys.* **13**, 15069 (2011).
37. Busch, M. Water oxidation: from mechanisms to limitations. *Curr. Opin. Electrochem.* **9**, 278–284 (2018).
38. Nong, H. N. et al. Key role of chemistry versus bias in electrocatalytic oxygen evolution. *Nature* **587**, 408–413 (2020).
39. Hess, F. & Over, H. Coordination inversion of the tetrahedrally coordinated Ru_{4f} surface complex on RuO_2 (100) and its decisive role in the anodic corrosion process. *ACS Catal.* **13**, 3433–3443 (2023).
40. Yu, S., Levell, Z., Jiang, Z., Zhao, X. & Liu, Y. What is the rate-limiting step of oxygen reduction reaction on Fe–N–C catalysts? *J. Am. Chem. Soc.* **145**, 25352–25356 (2023).
41. Exner, K. S., Usama, M., Razzaq, S. & Hattig, C. Oxygen evolution reaction on IrO2(110) is governed by Walden-type mechanisms. *Nat. Commun.* **16**, 6137 (2025).
42. Exner, K. S. A universal descriptor for the screening of electrode materials for multiple-electron processes: beyond the thermodynamic overpotential. *ACS Catal.* **10**, 12607–12617 (2020).
43. Razzaq, S. & Exner, K. S. Materials screening by the descriptor G_{max} (η): the free-energy span model in electrocatalysis. *ACS Catal.* **13**, 1740–1758 (2023).
44. Kozuch, S. & Shaik, S. How to conceptualize catalytic cycles? The energetic span model. *Acc. Chem. Res.* **44**, 101–110 (2011).
45. Kozuch, S. & Martin, J. M. L. The rate-determining step is dead. long live the rate-determining state!. *ChemPhysChem* **12**, 1413–1418 (2011).
46. McCrory, C. C. L., Jung, S., Peters, J. C. & Jaramillo, T. F. Benchmarking heterogeneous electrocatalysts for the oxygen evolution reaction. *J. Am. Chem. Soc.* **135**, 16977–16987 (2013).
47. Koper, M. T. M. Analysis of electrocatalytic reaction schemes: distinction between rate-determining and potential-determining steps. *J. Solid State Electrochem.* **17**, 339–344 (2013).
48. Campbell, C. T. Future directions and industrial perspectives micro- and macro-kinetics: their relationship in heterogeneous catalysis. *Top. Catal.* **1**, 353–366 (1994).
49. Campbell, C. T. The degree of rate control: a powerful tool for catalysis research. *ACS Catal.* **7**, 2770–2779 (2017).
50. Kresse, G. & Furthmüller, J. Efficient iterative schemes for ab initio total-energy calculations using a plane-wave basis set. *Phys. Rev. B* **54**, 11169–11186 (1996).
51. Sokolov, M. & Exner, K. S. Data repository and scripts for the DFT calculations of OER on pentlandite electrode materials. *Zenodo* https://doi.org/10.5281/zenodo.17554150 (2025).
52. Perdew, J. P., Burke, K. & Ernzerhof, M. Generalized gradient approximation made simple. *Phys. Rev. Lett.* **77**, 3865–3868 (1996).
53. Hammer, B., Hansen, L. B. & Nørskov, J. K. Improved adsorption energetics within density-functional theory using revised Perdew-Burke-Ernzerhof functionals. *Phys. Rev. B* **59**, 7413–7421 (1999).
54. Grimme, S., Antony, J., Ehrlich, S. & Krieg, H. A consistent and accurate ab initio parametrization of density functional dispersion correction (DFT-D) for the 94 elements H-Pu. *J. Chem. Phys.* **132**, 154104 (2010).
55. Grimme, S., Ehrlich, S. & Goerigk, L. Effect of the damping function in dispersion corrected density functional theory. *J. Comput. Chem.* **32**, 1456–1465 (2011).
56. Atkins, P. W. *Physical Chemistry* 6th edn (Oxford Univ. Press, 1998).
57. Drebushchak, V. A., Fedorova, Z.hN. & Sinyakova, E. F. Decay of (Fe1−xNix)0.96S DSC investigation. *J. Therm. Anal.* **48**, 727–734 (1997).
58. Mahlberg, D., Sakong, S., Forster-Tonigold, K. & Groß, A. Improved DFT adsorption energies with semiempirical dispersion corrections. *J. Chem. Theory Comput.* **15**, 3250–3259 (2019).
59. Göltl, F., Murray, E. A., Tacey, S. A., Rangarajan, S. & Mavrikakis, M. Comparing the performance of density functionals in describing the adsorption of atoms and small molecules on Ni(111). *Surf. Sci.* **700**, 121675 (2020).
60. Zeng, Z. et al. Towards first principles-based prediction of highly accurate electrochemical Pourbaix diagrams. *J. Phys. Chem. C.* **119**, 18177–18187 (2015).
61. Tesch, R. & Kowalski, P. M. Hubbard U parameters for transition metals from first principles. *Phys. Rev. B* **105**, 195153 (2022).
62. Yu, M. & Trinkle, D. R. Accurate and efficient algorithm for Bader charge integration. *J. Chem. Phys.* **134**, 064111 (2011).
63. Ali Akbari, M. S., Bagheri, R., Song, Z. & Najafpour, M. M. Oxygen-evolution reaction by nickel/nickel oxide interface in the presence of ferrate(VI). *Sci. Rep.* **10**, 8757 (2020).
64. Sargeant, E., Illas, F., Rodríguez, P. & Calle-Vallejo, F. Importance of the gas-phase error correction for O2 when using DFT to model the oxygen reduction and evolution reactions. *J. Electroanal. Chem.* **896**, 115178 (2021).
65. Urrego-Ortiz, R., Builes, S., Illas, F. & Calle-Vallejo, F. Gas-phase errors in computational electrocatalysis: a review. *EES Catal.* **2**, 157–179 (2024).
66. Liang, Q., Brocks, G. & Bieberle-Hütter, A. Oxygen evolution reaction (OER) mechanism under alkaline and acidic conditions. *J. Phys. Energy* **3**, 026001 (2021).
67. Sokolov, M. et al. Computational study of oxygen evolution reaction on flat and stepped surfaces of strontium titanate. *Catal. Today* **432**, 114609 (2024).

Acknowledgements

M.S. and K.S.E. acknowledge funding from the RESOLV Cluster of Excellence, funded by the Deutsche Forschungsgemeinschaft under Germany's Excellence Strategy—EXC 2033—390677874— RESOLV. M.S. and K.S.E. are thankful for fruitful discussions with Prof. Dr. Ulf-Peter Apfel (RU Bochum) on experimental investigations of pentlandite electrodes. This article is based on the work from COST Action 18234, supported by COST (European Cooperation in Science and Technology). M.S. acknowledges the support of the M-Era.Net project HetCat.

Author contributions

M.S.: Methodology, software, formal analysis, investigation, data curation, writing—original draft, writing—review and editing, and visualization. K.S.E.: Conceptualization, resources, writing—review and editing, supervision, project administration, and funding acquisition.

Funding

Open Access funding enabled and organized by Projekt DEAL.

Competing interests

The authors declare no competing interests.

Additional information

Supplementary information The online version contains supplementary material available at https://doi.org/10.1038/s41524-026-01961-x.

Correspondence and requests for materials should be addressed to Kai S. Exner.